Solid Earth, 7, 323–340, 2016
www.solid-earth.net/7/323/2016/
doi:10.5194/se-7-323-2016

Solid Earth Open Access EGU

3-D visualisation of palaeoseismic trench stratigraphy and trench logging using terrestrial remote sensing and GPR – a multiparametric interpretation

Sascha Schneiderwind[1], **Jack Mason**[1], **Thomas Wiatr**[2], **Ioannis Papanikolaou**[3], **and Klaus Reicherter**[1]

[1]Institute of Neotectonics and Natural Hazards, RWTH Aachen University, Lochnerstraße 4-20, 52056 Aachen, Germany
[2]Fundamental matters/Division GI, Federal Agency for Cartography and Geodesy, Richard-Strauss-Allee 11, 60598 Frankfurt am Main, Germany
[3]Laboratory Mineralogy – Geology, Agricultural University of Athens, Iera Odos 75, 11855 Athens, Greece

Correspondence to: Sascha Schneiderwind (s.schneiderwind@nug.rwth-aachen.de)

Received: 24 August 2015 – Published in Solid Earth Discuss.: 22 September 2015
Revised: 18 February 2016 – Accepted: 18 February 2016 – Published: 4 March 2016

Abstract. Two normal faults on the island of Crete and mainland Greece were studied to test an innovative workflow with the goal of obtaining a more objective palaeoseismic trench log, and a 3-D view of the sedimentary architecture within the trench walls. Sedimentary feature geometries in palaeoseismic trenches are related to palaeoearthquake magnitudes which are used in seismic hazard assessments. If the geometry of these sedimentary features can be more representatively measured, seismic hazard assessments can be improved. In this study more representative measurements of sedimentary features are achieved by combining classical palaeoseismic trenching techniques with multispectral approaches. A conventional trench log was firstly compared to results of ISO (iterative self-organising) cluster analysis of a true colour photomosaic representing the spectrum of visible light. Photomosaic acquisition disadvantages (e.g. illumination) were addressed by complementing the data set with active near-infrared backscatter signal image from t-LiDAR measurements. The multispectral analysis shows that distinct layers can be identified and it compares well with the conventional trench log. According to this, a distinction of adjacent stratigraphic units was enabled by their particular multispectral composition signature. Based on the trench log, a 3-D interpretation of attached 2-D ground-penetrating radar (GPR) profiles collected on the vertical trench wall was then possible. This is highly beneficial for measuring representative layer thicknesses, displacements, and geometries at depth within the trench wall. Thus, misinterpretation due to cutting effects is minimised. This manuscript combines multiparametric approaches and shows (i) how a 3-D visualisation of palaeoseismic trench stratigraphy and logging can be accomplished by combining t-LiDAR and GPR techniques, and (ii) how a multispectral digital analysis can offer additional advantages to interpret palaeoseismic and stratigraphic data. The multispectral data sets are stored allowing unbiased input for future (re)investigations.

1 Introduction

Seismic hazard assessment is still predominantly based on the instrumental and historical catalogues of seismicity. However, these catalogues are generally too short compared to the recurrence interval of particular faults (e.g. Wesnousky, 1986; Yeats and Prentice, 1996; Machette, 2000). As a result, the sample from the statistical elaboration of the historical and instrumental data is incomplete and a large number of faults would have not ruptured during the period where the historical record is considered complete (Stucchi et al., 2004, 2013; Woessner and Wiemer, 2005; Guidoboni and Ebel, 2009; Grützner et al., 2013; Papanikolaou et al., 2015). The need for fault-specific studies and the extraction of recurrence intervals from palaeoseismological trenches was then initiated in the late 1970s (Sieh, 1978; McCalpin, 2009). The goal is to extend the history of slip on a fault back many thousands of years, a time span that generally encompasses

a large number of earthquake cycles (Yeats and Prentice, 1996).

Over the last few years, fault-specific studies and palaeoseismology have been further advanced and are now supported by new remote sensing tools that offer high spatial resolution (e.g. LiDAR) and geophysics that extend our data into the subsurface (ground-penetrating radar, GPR; electric resistivity tomography, ERT) (Papanikolaou et al., 2015). This manuscript adds to such approaches and shows (i) how a 3-D visualisation of palaeoseismic trench stratigraphy and logging can be accomplished by combining t-LiDAR and GPR techniques, and (ii) how a multispectral digital analysis can offer additional advantages and a higher objectivity in trench data interpretation.

Palaeoseismological studies are often undertaken to identify earthquake recurrence intervals and maximum credible magnitudes of prehistoric earthquakes (McCalpin, 2009). These parameters are needed for the accurate calculation of seismic hazard potential of active fault zones (Reicherter et al., 2009). Evidence for palaeoearthquakes can be found within the sedimentary architecture of active faults where conditions are favourable for their preservation. Typical features caused by recurrent seismic events include (i) progressive displacements (Keller and Rockwell, 1984), (ii) colluvial wedges, (iii) liquefaction, and (iv) fissure fills (Reicherter et al., 2003; Kokkalas et al., 2007; McCalpin, 2009) (see Fig. 1d). The geometry and stratigraphic position of these features allow a retrodeformation of recurrent surface-rupturing events, whereas carbon rich material can be used to date prehistoric earthquakes and determine recurrence intervals. To access these potential archives of seismic information, trenches, which are often expensive in terms of, for example, their approval, excavation, groundwater pumping, and shoring, are excavated across deformation zones. Then, the classical approach is to document stratigraphy and structure by careful logging, either on paper and/or with photographs (e.g. Wallace, 1986; McCalpin, 2009). The accuracy of the trench log is dependent on the logger's experience and ability to define units of discrete deposits that have distinguishable lithological characteristics compared with adjacent deposits.

Palaeoseismic indicators are widely spread and their formation varies along fault strike (e.g. Bubeck et al., 2015). For this reason, geophysical surveys undertaken prior to the trenching phase have become common practice over the last decade. For instance, ground-penetrating radar (GPR) measurements have been carried out to identify optimum trenching locations (e.g. Demanet et al., 2001; Alasset and Meghraoui, 2005; Grützner et al., 2012) and many studies have shown that earthquake-related structures can be identified in the shallow subsurface with geophysics (e.g. Chow et al., 2001; Reiss et al., 2003; Bubeck et al., 2015). The excavated trench wall is then a 2-D representation of the fault zone stratigraphy. It is assumed that the 2-D geometry of the logged sedimentary features continues along strike either side of the trench; without widening the trench along strike, or excavating more trenches, we must assume that the 2-D trench log is representative for this location along the fault. Hence, an interpretation of a 2-D exposure of very local variations and/or accumulations of colluvial deposits yield results different from statistical significance which gets closer to the real-world conditions. Trenches target predominantly palaeosols on either side of the fault, and then according to empirical relationships (Wells and Coppersmith, 1994), palaeomagnitudes can be estimated based on these coseismic displacements. If no or only poorly expressed displaced palaeosols exist, the geometry of sedimentary features within trenches is used to estimate previous earthquake displacements. As a rule of thumb, colluvial wedge thickness equals half of the initial scarp height (e.g. Reicherter, 2001; Reiss et al., 2003; McCalpin, 2009). Such information is then used as input parameters for seismic hazard assessment. Therefore, tracing the geometry of these features is essential for the most accurate seismic hazard calculations. A better visualisation can improve the definition of separate unit boundaries and features, offering better interpretations and limiting uncertainties.

In this study we demonstrate how high-resolution t-LiDAR (terrestrial light detection and ranging) measurements and photomosaics can be used to assist in the interpretation of palaeoseismological exposures; we also show how an accurately arranged 2-D GPR survey can assist in visualising sedimentary structures in 3-D (e.g. Vanneste et al., 2008; Christie et al., 2009; Ercoli et al., 2013) within the trench wall. The t-LiDAR's backscatter signal represents material reflectance of radiation in the near-infrared wavelength, and digital photo cameras collect information of the reflectance of visible light; therefore, a quasi-multispectral inspection of the exposures is possible. Ragona et al. (2006) developed a method using imaging spectroscopy on palaeoseismic exposures with hyperspectral and normal digital cameras. As an outcome they were able to enhance the visualisation of the sedimentary layers and other features that are not obvious or even not visible to the human eye. Another study undertaken by Wiatr et al. (2015) places emphasis on the use of the monochromatic laser beam's backscattered signal to determine varying surface conditions. Using these techniques we assist experienced-based trench logging and obtain 3-D spectral data to support the interpretation of palaeoseismological deposits. Two-dimensional GPR surveys, arranged for a pseudo-3-D cube reconstruction, undertaken on top of the trench and on the vertical trench wall (Fig. 2), are used in combination with a high-resolution digital elevation model (DEM) from t-LiDAR scanning. This allows radar facies (Neal, 2004) to be distinguished and the sedimentological architecture at depth within the trench wall to be identified. Thus, the resulting 3-D model from the GPR provides information on varying layer thicknesses and minimises misinterpretation due to cutting effects. The workflow comprising data acquisition, statistical analysis, interpretation, and

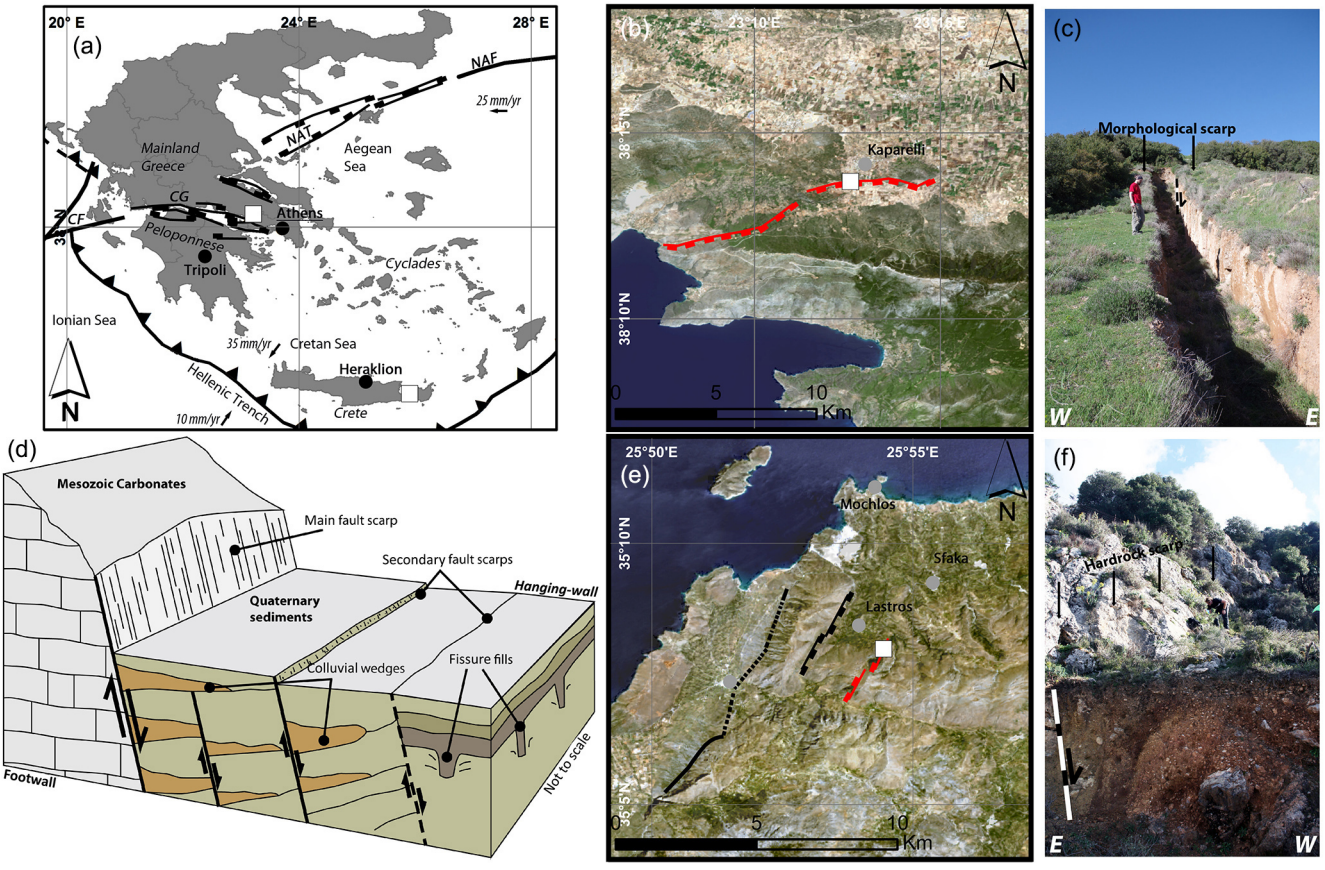

Figure 1. Guide to the study area. **(a)** Map of Greece showing simplified large-scale tectonic structures (CG, Corinthian Gulf; CF, Cephalonia Fault; NAF, North Anatolian Fault; NAT, North Aegean Trough; black lines with barbs show active thrusts; black lines with marks show active faults) (after Kokkalas and Koukouvelas, 2005; Papanikolaou and Royden, 2007). White boxes highlight study areas. **(b)** Satellite image (Landsat 8, 2015) of the easternmost Gulf of Corinth. The Kaparelli Fault is shown in red and the white box marks the position of the palaeoseismological trench of Kokkalas et al. (2007). **(c)** View of the Kaparelli trench. **(d)** Satellite image (Landsat 8, 2015) of the study area at the Sfaka Fault (red) in northeastern Crete; the white box shows the position of the road cut along strike. **(e)** View of the Sfaka road cut. **(f)** Sketch of a typical postglacial normal fault showing bedrock juxtaposed against Quaternary sediments which contain structures caused by recurrent earthquakes (modified after Reicherter et al., 2003). Colluvial wedges form at the base of the fault scarp from eroded material originating at the top of the scarp.

storage (Fig. 3) was calibrated on a road cut on the island of Crete. We then applied this workflow on a professionally excavated trench in mainland Greece.

2 Geological setting of the study sites

The study sites are both located in Greece, which is one of the most seismically active parts of the Mediterranean (McKenzie, 1972; Le Pichon and Angelier, 1979; Papazachos et al., 2000) due to the presence of the Hellenic arc and trench system. Crustal extension orientated both arc-parallel and arc-perpendicular (Mariolakos and Papanikolaou, 1981; Lyon-Caen et al., 1988) has led to the development of Quaternary carbonate bedrock fault scarps throughout both mainland Greece (Stewart and Hancock, 1991; Benedetti et al., 2002) and the island of Crete (e.g. Gaki-Papanastassiou et al., 2009). These normal faults mainly consist of footwall Mesozoic carbonates juxtaposed against hanging-wall flysch and/or post-alpine sediments. Earthquake features such as colluvial wedges (a consequence of degradation of the scarp), fissure fills, and displaced strata occur within the hanging walls of these faults and datable material may be contained within buried palaeosols (see Fig. 1d) (McCalpin, 2009). To create those archives and preserve them over geological timescales, erosional processes must be lower than the rate of tectonic activity. These features therefore represent geological archives of palaeoearthquakes because they can record information about Holocene and Late Pleistocene earthquakes (e.g. McCalpin, 2009). Ambraseys and Jackson (1990) estimate that a maximum earthquake magnitude of $M_s = 7.0$ could occur on these normal faults using macroseismic and instrumental data, which coincides with

fault segment lengths of 15–30 km (Wells and Coppersmith, 1994).

2.1 The Sfaka Fault (NE Crete, Greece)

The island of Crete is the largest within the Greek territory and is directly adjacent to the subduction zone between Europe and Africa. The NNE–SSW-trending Sfaka Fault is located in northeastern Crete (Fig. 1a) and forms the easternmost segment within the Ierapetra Fault Zone which is a major tectonic line of approximately 25 km cutting through the whole island (Gaki-Papanastassiou et al., 2009). This northwest dipping normal fault is easy to recognise as a prominent fault scarp of up to 6 m. The scarp dips 70° towards the west and offsets smooth mountain slopes for approximately 5 km onshore (Fig. 1e). Together with the opposing Lastros fault, a 2 km wide graben structure is formed.

An outcrop in the form of a dirt road cut (located at 35°7′58.97″ N, 25°54′26.01″ E) exhibits the fault zone as a contact between footwall Mesozoic carbonates and hanging-wall colluvium (Fig. 1f). The outcrop cuts the fault at an angle of approximately 75° from the fault strike.

2.2 The Kaparelli Fault (Gulf of Corinth, Greece)

The Kaparelli Fault is located in the easternmost part of the Gulf of Corinth (see Fig. 1a) which is associated with rapid extension oriented N–S (e.g. Papanikolaou and Royden, 2007). The Kaparelli Fault became well known as it ruptured during the 1981 Corinthian Alkyonides earthquake sequence in February (24th, $M_s = 6.7$, depth: 10 km; 25th, $M_s = 6.4$, depth: 8 km) and March (4th, $M_s = 6.4$, depth: 8 km) (Jackson et al., 1982). Many palaeoseismological studies using various approaches have been undertaken along this ca. 20 km long south-dipping normal fault. For example Benedetti et al. (2003) used ^{36}Cl cosmic ray exposure dating to determine the history of surface-rupturing events on the 4–5 m high limestone scarp of the Kaparelli Fault. Their results show evidence for seismic activity 20 ± 3, 14.5 ± 0.5, and 10.5 ± 0.5 ka prior to the 1981 earthquake sequence. A palaeoseismological trenching study was conducted by Kokkalas et al. (2007). The authors found evidence for at least three events in the past 10 000 years: 9370 ± 120, 7290 ± 140 to 5640 ± 70, and 1225 ± 165 years. The excavations from Kokkalas et al. (2007) are still open; therefore, the already logged and interpreted structures within trench Kap-1 (Fig. 1f) represent a perfect site to test remote sensing data acquisition.

3 Methodology

The herein presented workflow comprises (i) a combination of conventional trench logging and remote sensing measurements, (ii) a comparison of common photographs and near-infrared images, and (iii) a GPR survey (Fig. 3). It combines palaeoseismic trenching techniques with t-LiDAR measurements to improve the accuracy of palaeoearthquake reconstruction. A multispectral analysis of t-LIDAR backscatter data and the luminescence of true colour photographs were compared to the manual trench log. A GPR survey was then conducted to obtain 3-D information of layer continuation and thickness at depth within the trench wall (Fig. 2).

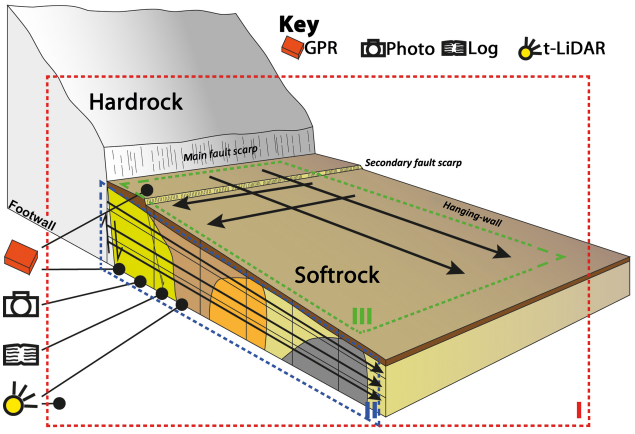

Figure 2. A simplified model of investigated parts on footwall, scarp, hanging wall, and trench at both exposures of this study; visualisation shows the conditions at the Sfaka road cut. Dashed lines show the different work spaces: (I) red, overall workspace for a long–mid-range t-LiDAR scan to retrieve the geometric relation of investigated components; (II) blue, area of operations (log, photo, t-LiDAR, GPR) on the trench wall; (III) green, workspace for GPR measurements (black arrows) on top of the colluvium.

3.1 Conventional trench logging and photomosaic

A palaeoseismic trench is characterised by the subsurface exposure of fault zones and deformed stratigraphy. To accurately interpret these features, apparent dips and anthropogenic and/or exogenous influences must be excluded. Moreover, sketching lithological contents requires an exposure devoid of weathered and smeared parts that were caused by the excavation (McCalpin, 2009). To simplify and prove the geometrical correctness of the trench log, a reference grid of 1 m^2 was attached to the wall. The grid's points of intersection also act as reference points for remote sensing applications (Reitman et al., 2015).

The trenches were logged in 1 : 10 scale. Thereby, discrete deposits that are composed of similar lithology considering consistent texture, sorting, bedding, fabric, and colour of individual layers are mapped. Photographs of every square metre were taken and later stitched together using an automatic panorama recognising tool including a manual editor of control points and straightening functions (Autopano Giga, Kolor). It must be noted that error values are already stored within image information due to differing luminous exposures; furthermore, holes and protruding boulders create

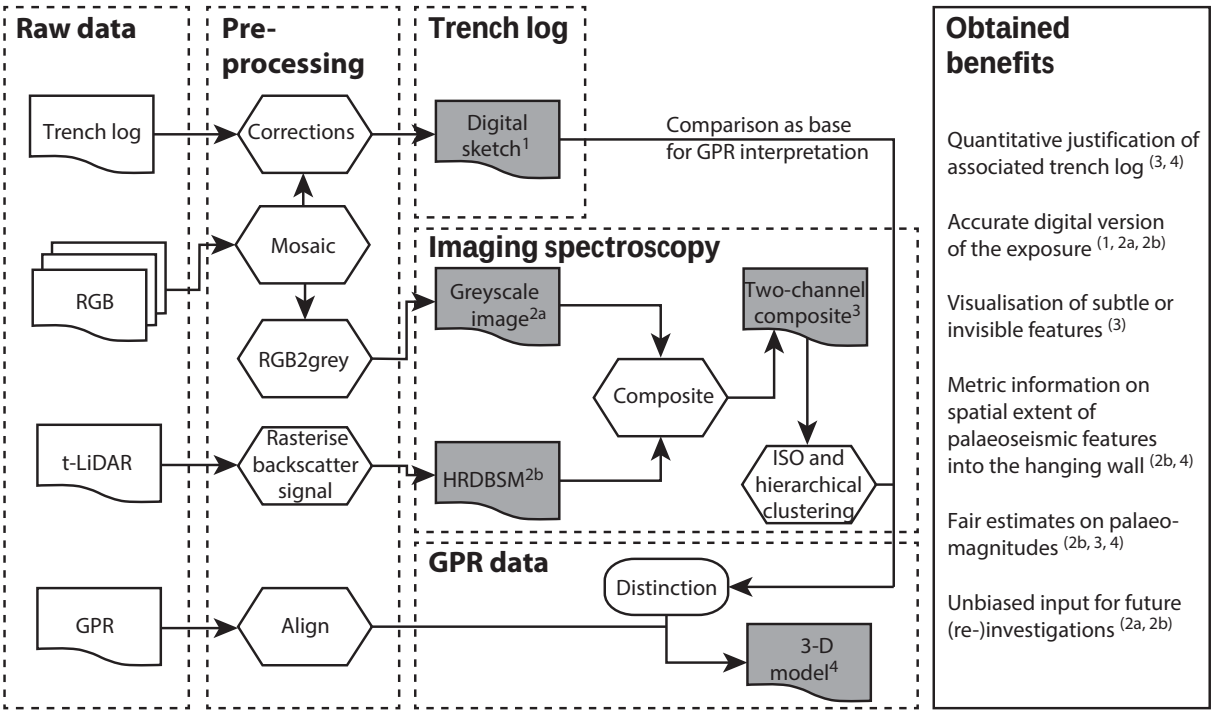

Figure 3. Flowchart of conventional trench logging, imaging spectroscopy and GPR survey; their comparison and combination. Palaeoseismological studies benefits from one or multiple data sets (grey) generated with this workflow.

shadows that partially change the reflection characteristics of certain sedimentological features. The Sfaka road cut faces north (see Fig. 1e and f) and is surrounded by steep slopes. Since footwall and hanging-wall deformation structures are exposed, the outcrop is a suitable palaeoseimological trench after manual levelling and deepening of the most interesting parts. In Kaparelli the eastern trench wall (see Fig. 1b and c) was investigated because it preserved the best stratigraphy and exhibits clear horizons of multiple faulting events (Kokkalas et al., 2007). To avoid most of the differing luminous exposures, the photographs were either taken in the morning when the angle of sunlight was shallow and did not shine directly onto the investigated wall (Kaparelli trench) or in the afternoon when the sun disappeared behind the surrounding hills (Sfaka road cut).

The photomosaic of true colour images (red, green, blue; RGB method) was converted into a greysacle image to eliminate hue and saturation information while retaining the luminance (0–255) using the rgb2gray function in MATLAB®. In a geographical information system (GIS), the resulting image was geo-referenced to a custom frame in order to make it comparable to all other data sets of this study.

3.2 t-LiDAR measurements

t-LiDAR (terrestrial Light Detection and Ranging) is a remote sensing technique with high spatial and temporal resolution and is a very effective instrument for reconstructing morphology (Brodu and Lague, 2012, Wilkinson et al., 2015), geological settings, and monitoring movements (Jones, 2006; Hu et al., 2012). In seismic hazard assessment, this technology assists fault mapping (e.g. Arrowsmith and Zielke, 2009; Begg and Mouslopoulou, 2010) as well as providing a tool to trace palaeoevents based on changes in reflectivity and roughness on fault scarps (Wiatr et al., 2015). A generated coherent laser beam with little divergence by stimulated emission is reflected off surfaces and the proportionate backscattered signal is detected, forming a non-contact and non-penetrative active and stationary recording system. Thus, from measuring the two-way travel time (TWT) of a first-pulse detection sequence, 3-D surface data are acquired. The illuminated area is controlled by wavelength, beam divergence, range between sensor and target, and also by the angle of incidence (Jörg et al., 2006; Wiatr et al., 2015). In our study we used an ILRIS 3-D laser ranging system (wavelength λ is 1500 nm) from OPTECH Inc., Ontario, Canada.

The limitations of using t-LiDAR are high humidity (e.g. Lobell and Asner, 2002) and low target reflection with cumulative distance and shallow incident angle (e.g. Höfle and Pfeifer, 2007). In order to assume constant soil moisture and to ensure the backscatter signal data quality, close-range scans were done during the summer in dry conditions within a few hours. The scans were carried out almost perpendicular to the trench wall. Since the Kaparelli trench is too narrow for scans from inside, the data were collected from outside of

the excavation. At the Sfaka Fault road cut, scans were undertaken at 5 m distance.

Other benefits of applying t-LiDAR is its flexibility, the relatively quick availability of an actual data set, and also its high spatial resolution with information about backscatter signal each referenced in x, y, z coordinates. The result is an irregular but dense point cloud representing a highly detailed digital 3-D surface model which can be easily implemented in GISs to generate accurate DEMs or digital terrain models (e.g. Wiatr et al., 2015).

For this study, the t-LiDAR scanning was undertaken at both close range and long–mid-range to determine geometrical relationships between the footwall, hanging wall, prolongation of the scarp, and trench wall (see Fig. 2). The backscatter signal of the t-LiDAR results from the reflection of transmitted waves of near-infrared light. In other words, each measurement is usually accompanied by a surface remission value, which quantifies the intensity of the reflected laser beam. The monochromatic backscatter signal values are stored as greyscale values from 0 to 255. The information on the monochromatic wavelength and the detected backscattered signal in the near-infrared reflects the surface properties which are invisible to the human eye. Thus, the backscatter signal was also used for the multispectral analysis. The raw data were cleaned from isolated points and those that do not represent the area of interest. The mathematical and geometrical alignment of the different scan windows was then carried out. For project-specific demands, the data sets were translated into a custom grid. The long–mid-range data were used for the overall geometrical analysis, creating high-resolution DEMs with a resolution smaller than 0.1 m. Data from the close-range scan were processed for statistical calculations of the backscatter signal's spatial distribution. A detailed description of the applied workflow is given in Sect. 3.3.

3.3 Imaging spectroscopy

Visualising an array of simultaneously acquired images that record separate wavelength intervals or bands is part of multispectral analyses. A common multispectral camera employs a range of film and filter combinations to acquire photographs that record narrow spectral bands of non-imaging data. Reflectance spectra map the percentage of incident energy (e.g. sunlight) that is reflected by a material as a function of energy wavelength. Absorption of incident energy is represented by downward excursions of a curve (absorption features). Upward excursions represent superior reflectance (reflectance peaks). These features are valuable clues for recognising and distinguishing certain materials (Sabins, 1997). Multispectral imaging, or imaging spectroscopy, has been used at many different scales for remote sensing. Probably the most prominent example for macro-scale investigations is the inspection of visible and near-infrared satellite imagery for mapping and monitoring vegetation (e.g. Tucker, 1979). Ragona et al. (2006) introduced an application of high-resolution field imaging spectroscopy on palaeoseismic exposures using hyperspectral and common digital photo cameras. The authors conclude that imaging spectroscopy can be successfully applied to assist in the description and interpretation of palaeoseismic exposures because (i) subtle or invisible features are displayed, (ii) quantitative analysis and comparisons of units using reflectance spectra can be undertaken, and (iii) unbiased data are stored for future access and analysis.

The limitations of multispectral approaches are, by their nature, closely connected to the application of photomosaics and t-LiDAR measurements. We re-emphasise the influence of moisture; where present it not only causes a darkening of the sediments (reduction in reflectance), but there is also a hard-to-quantify content variation across the exposure (Ragona et al., 2006). Another error source appears due to morphological characteristics of a certain exposure, especially on surfaces that are not well prepared for palaeoseismic investigations and data collection. This means that the exposure must be flattened and cleaned to avoid changes in spectral amplitudes accompanying changes in illumination angle and distance.

We assume that the moisture content was similar throughout the exposure, and water absorptions should not affect the correlations because the spectral change is similar along the trench wall. Furthermore, the photos and t-LiDAR scans were taken almost perpendicular to the exposure so that optimal data quality can be expected.

The workflow consists of geo-referencing and snapping the high-resolution raster data from the photomosaic and t-LiDAR backscatter signal to a coherent cell size (0.001 m) in GIS. Afterwards, an ISO (iterative self-organising) cluster unsupervised classification was applied to a two-channel composition of both raster layers. Thereby, the number of classes was set to 10 times the number of included bands (photomosaic grey-level image and t-LiDAR backscatter signal image) as this provides sufficient statistics and enough cells to accurately represent a certain cluster. This type of clustering uses a process in which all samples are assigned to existing cluster centres during each iteration; new means are then recalculated for every class. The actual number of classes is usually unknown; therefore, we started with 20 classes and analysed the attribute distances between sequentially merged classes with the dendrogram method (hierarchical clustering). This reduces statistical misclassifications and provides information on distinct classes. Based on the outcome, classes which are statistically closest get merged and the data set gets reclassified. Block statistics within a 3×3 cell environment are applied to erase noise by overwriting cell values to all of the cells in each block with the median value (Fig. 4). Moreover, resampling down to 0.02 m cells enhances visibility and allows a more general interpretation and comparison to the conventional log. This is because the scattered signal gets reduced so there is

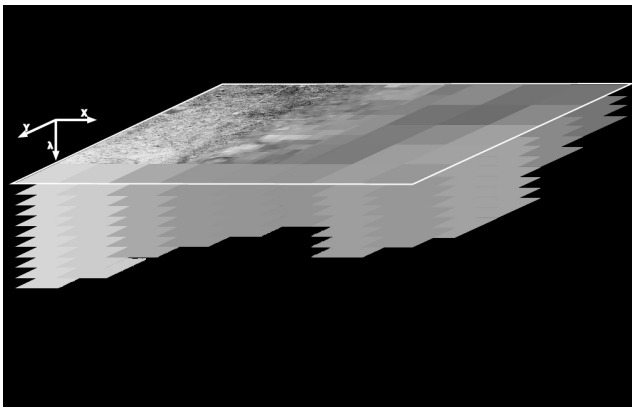

Figure 4. An illustration showing how spatial information gets down-sampled. The median value of surrounding cells provides the new cell (x, y) value (λ).

less influence by local variations. The threshold is chosen because average gridding and sketching inaccuracy is around 2 % (McCalpin, 2009).

3.4 Ground-penetrating radar

GPR is a non-invasive and non-destructive geophysical technique that operates with high-frequency electromagnetic waves in the radio band to detect electrical discontinuities in the shallow subsurface up to approximately 50 m. Every GPR measurement contains a five-step process of (i) generating, (ii) transmitting, (iii) propagating, (iv) reflecting, and (v) receiving electromagnetic pulses. The differing relative dielectric permittivities (εr) of varying materials control the transmitting velocity in relation to the speed of light ($c = 0.2998\,\mathrm{m\,ns^{-1}}$) once the pulse is emitted from the antenna. Fractional reflections of the pulse on inhomogeneities and layer boundaries get received due to a dielectric contrast. In order to calculate depths of reflection the TWT is recorded in the order of nanoseconds. Depending on the frequency of the antenna, objects smaller than 0.1 m in diameter can be resolved. Common GPR systems perform at frequencies between 50 MHz and 1 GHz, where achievable resolution is a quarter of the wavelength. The relationship between penetration depth and spatial resolution is an inverse one; hence, a higher spatial resolution occurs at the expense of penetration depth and vice versa (Neal, 2004; Schrott and Sass, 2008).

Water is almost the only limiting parameter for the application of GPR because of its high relative dielectric permittivity. Moisture content dramatically decreases the electromagnetic wave velocity by stronger attenuation and leads to reduced penetration depths (Schrott and Sass, 2008). Soil moisture differences often severely disrupt wave energy, which makes it even more difficult to interpret reflections. Dielectric contrasts are the main features of the GPR image interpretation, since any dielectric discontinuity is detected. Thus, targets can be classified according to their geometry and reflection facies.

GPR was carried out on the vertical trench wall and on the slope surface above the trench (see Fig. 2). At the Sfaka Fault road cut, three horizontal profiles were collected on the vertical exposure with 0.3 m spacing between profiles. Fifteen profiles were collected on top of the trench in a grid array to obtain a high-resolution pseudo-3-D cube. At the Kaparelli trench, 20 profiles were collected on the vertical trench wall, and 14 on top of the hanging wall. In order to make the GPR operationally effective, our survey provided efficient coupling of the antenna to the ground and a sufficiently large scattered electromagnetic signal for detection at or above the ground surface. A 400 MHz antenna together with a SIR-3000 control unit from Geophysical Survey Systems Inc. (GSSI, Salem, NH, USA) was used to obtain desired resolution and noise levels. The data processing was done using the software ReflexW® (Sandmeier Scientific Software, Karlsruhe, Germany) involving the following processing sequence: remove header gain, move start time, energy decay, 1-D bandpass frequency, background removal, and average xy. Reflection hyperbolae of gravels were used to estimate wave velocity. Data migration was undertaken to correct angles, because dips are usually underestimated due to a complex 3-D cone in which electromagnetic energy radiates (Neal, 2004).

Based on the layers distinguished in the trench log and taking into account the results of the multispectral analysis, GPR data were then used to interpret the outcropping strata in 3-D.

4 Results

4.1 Sfaka Fault, Crete

4.1.1 Trench log

The trench was logged and 10 distinct layers were recognised. These vary in colour, matrix, and geometrical alignments. The trench exposes the limestone footwall at its eastern end between 0 and 1 m. The limestone is heavily weathered and degraded, both within and above the trench. Adjacent to the bedrock fault plane is fault gouge, which is approximately 1 m in thickness. However, true thickness is calculated to be around 0.8 m when correcting for the trench's strike 75° from the fault. The western end of the gouge is the primary fault contact. Here, the clasts within the gouge are aligned vertically and there is an abrupt contact to the next units. These units are interpreted as fissures filled with palaeosols (Fig. 5a). palaeosol 1 comprises light brown to reddish brown very gravelly silty clay with occasional cobbles and containing roots and rootlets, and palaeosol 2 comprises light brown to brown gravelly clay containing rare cobbles. Both of these palaeosols have high clay contents and

there is a sharp contact with the colluvial layers further to the west. The remaining sediments within the trench are colluvial deposits C1–C6. C1 is cemented colluvium located at the western end of the trench. C2–C6 are individual colluvial layers which can be traced from the cemented colluvium to the fissure fills. These colluvial layers are offset by a number of small displacement secondary faults. These minor faults are typical of extension in unconsolidated sediments.

The trench is not dominated by scarp-derived colluvial wedges formed after rupturing events. Instead earthquake evidence comes in the form of fissure fills which have developed within the hanging wall adjacent to the fault gouge (Fig. 5b). These fissure fills are filled with palaeosols and are faulted against colluvial material which is partly scarp-derived and partly hanging-wall-derived. Due to the nature of the sloping hanging wall and the location of both trenches, we believe that the main source of colluvial layers C2–C6 is hanging-wall colluvium from the south at higher elevations. This is also evidenced by the alluvial/colluvial fan located 85 m to the west of the trench. Two displacement events can be inferred based on fissure fill and colluvial stratigraphy. Dip–slip faulting causes the hanging wall to be downthrown and tilted; due to a slightly concave fault plane below the trench site, a tectonic fissure then opens up between the fault gouge and colluvial layers, and tilting is taken up on the small displacement antithetic faults within the colluvial layers. The fissure was then filled with scarp-derived and local hanging-wall material. The slope surface then stabilises, allowing gravelly topsoil to accumulate. The second displacement event then occurs and the above described process is repeated.

4.1.2 Imaging spectroscopy analysis

The greyscale photomosaic stores visual impressions in a way similar to the human eye and represents a weighted sum value of luminance within the range of visible light per pixel. Luminance at 1500 nm detected by t-LiDAR significantly differs in some parts of the trench wall (Fig. 5b, c). As shown in Table 1, the light fault gouge material is highly reflective in both photomosaic and high-resolution digital backscatter model (HRDBSM).

The homogeneous silty layer (fault gouge) contains only a few voids due to excavation works that influence reflectance value range. Resultant colorimetric shift expressed by the two-component composition almost solely depicts the highest value ranges for this part of the trench wall (Fig. 5d). In contrast, the cemented colluvium to the west is highly irregular in the sense of reflectance. Both the photomosaic and HRDBSM show a heterogeneous greyscale value distribution that is even more embodied by high-grade contrasts in the two-channel composition. Similar observations occur for larger boulders that protrude out of the trench wall (Fig. 5a, b, c, d).

Table 1. Median greyscale values of photomosaic, high-resolution digital backscatter model (HRDBSM), and two-component composition per stratigraphic unit from the trench log. The composition is the result of allocation of photomosaic and HRDBSM in equal parts, to visualise certainties and their variation within given zones. Error is given by single standard deviation.

Layer	Photomosaic	HRDBSM	Composition
Recent topsoil	132 ± 21	197 ± 12	138 ± 23
Fault gouge	221 ± 19	239 ± 12	224 ± 23
Palaeosol I	165 ± 19	170 ± 13	87 ± 23
Palaeosol II	156 ± 19	192 ± 10	128 ± 21
C6	131 ± 19	178 ± 10	99 ± 21
C5	152 ± 21	199 ± 11	142 ± 21
C4	143 ± 22	198 ± 10	140 ± 21
C3	171 ± 19	200 ± 12	144 ± 24
C2	147 ± 22	186 ± 13	116 ± 25
C1	144 ± 18	199 ± 15	144 ± 30
Boulder	168 ± 26	177 ± 15	102 ± 26

Colluvial layers C2–C5 are distinctively different in their reflectance characteristics. Where transition between both units is indeed visible in the photomosaic, a sharp contrast in reflectance characteristics of near-infrared is recognisable. Moreover, the named colluvial deposits do not only appear as a collection of diffuse values but show evidence of alignments. An upward-oriented structure of approximately 0.5 m thickness is obvious in the HRDBSM and false colour composition. The structure follows a secondary fault within the colluvial strata.

Figure 6 visualises percentages of seven classes, estimated from the unsupervised classification on individual identified layers within the trench log. Either the majority of a certain layer is fulfilled by one single class or by a certain composition of two or three classes. Where Table 1 shows the dominance of high values within the fault gouge layer, the illustration of unsupervised classification proves this layer to be almost completely (70 %) represented by one single class (7). Although class 4 covers almost the same value range as class 7, fault gouge exposure is only covered by 8 % by class 4 (see Fig. 6a).

In the unsupervised classification, the fault gouge is the only layer in this trench wall where the majority is covered by one single class. Palaeosols I and II have a similar ratio of effecting classes but class 6 is not present in the palaeosol II signature, allowing them to be differentiated. By visualising the spatial arrangement of influencing classes the differentiation between these two layers is even better (Fig. 5e). While Fig. 6b only shows percentage significance of class ratios per layer, the spatial distribution promotes the reconstruction of a certain layer. The accumulation of class 5 especially in the lower part of palaeosol I is obviously different from any other cluster in palaeosol II, although quantitative statistics conclude a similar composition of classes.

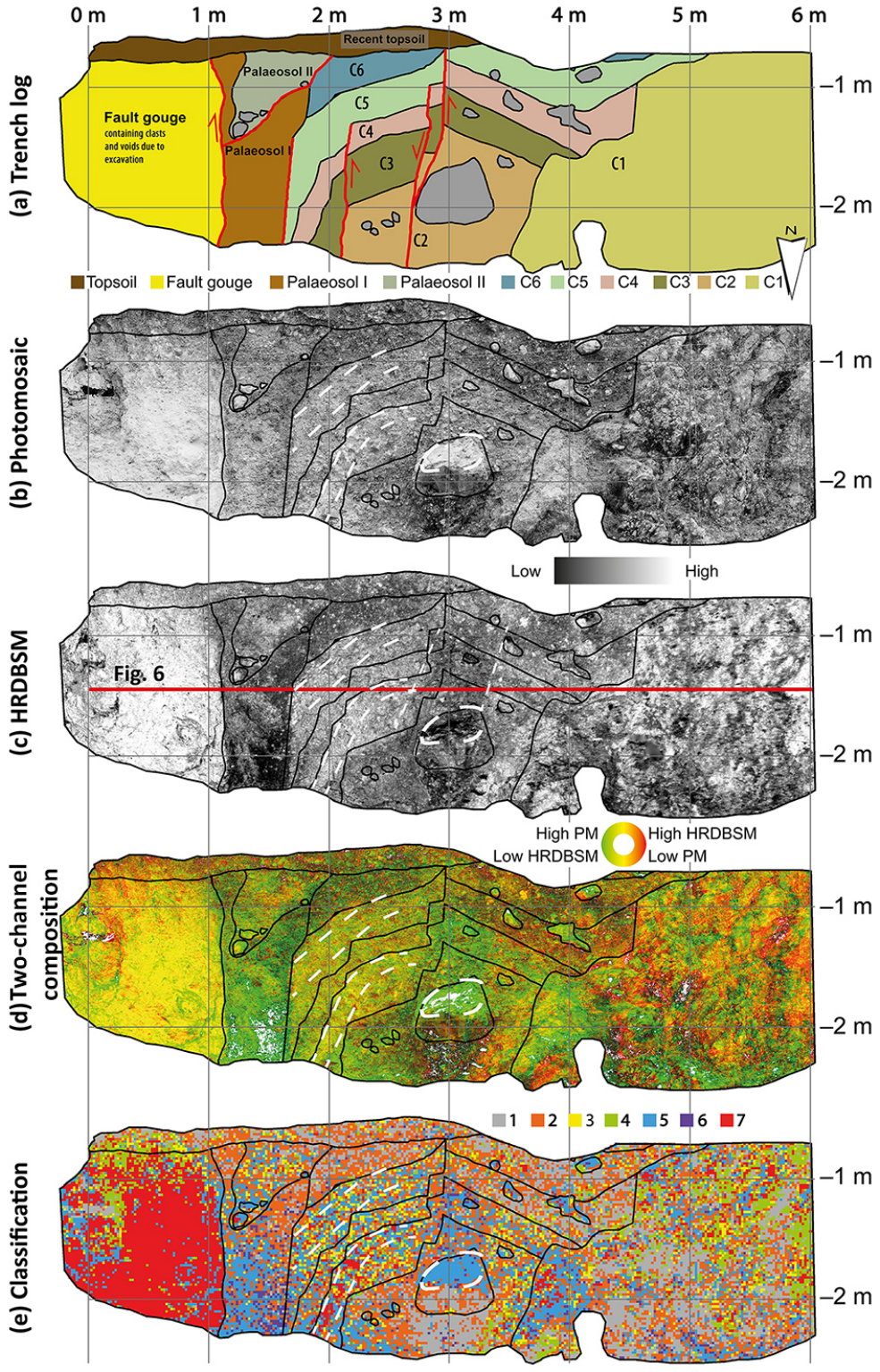

Figure 5. Compilation of analytical input and outcome at the Sfaka Fault road cut. **(a)** Trench log produced in the field and corrected with **(b)** photomosaic in the office. **(c)** High-resolution digital backscatter model (HRDBSM) from t-LiDAR measurements. **(d)** Two-channel composition from **(b)** and **(c)**. Note, green and red are 100 % different (PM denotes photomosaic). **(e)** Visualisation of spatial distribution of seven classes from the unsupervised classification. White dashed lines indicate coinciding arrangements and some influence from daylight.

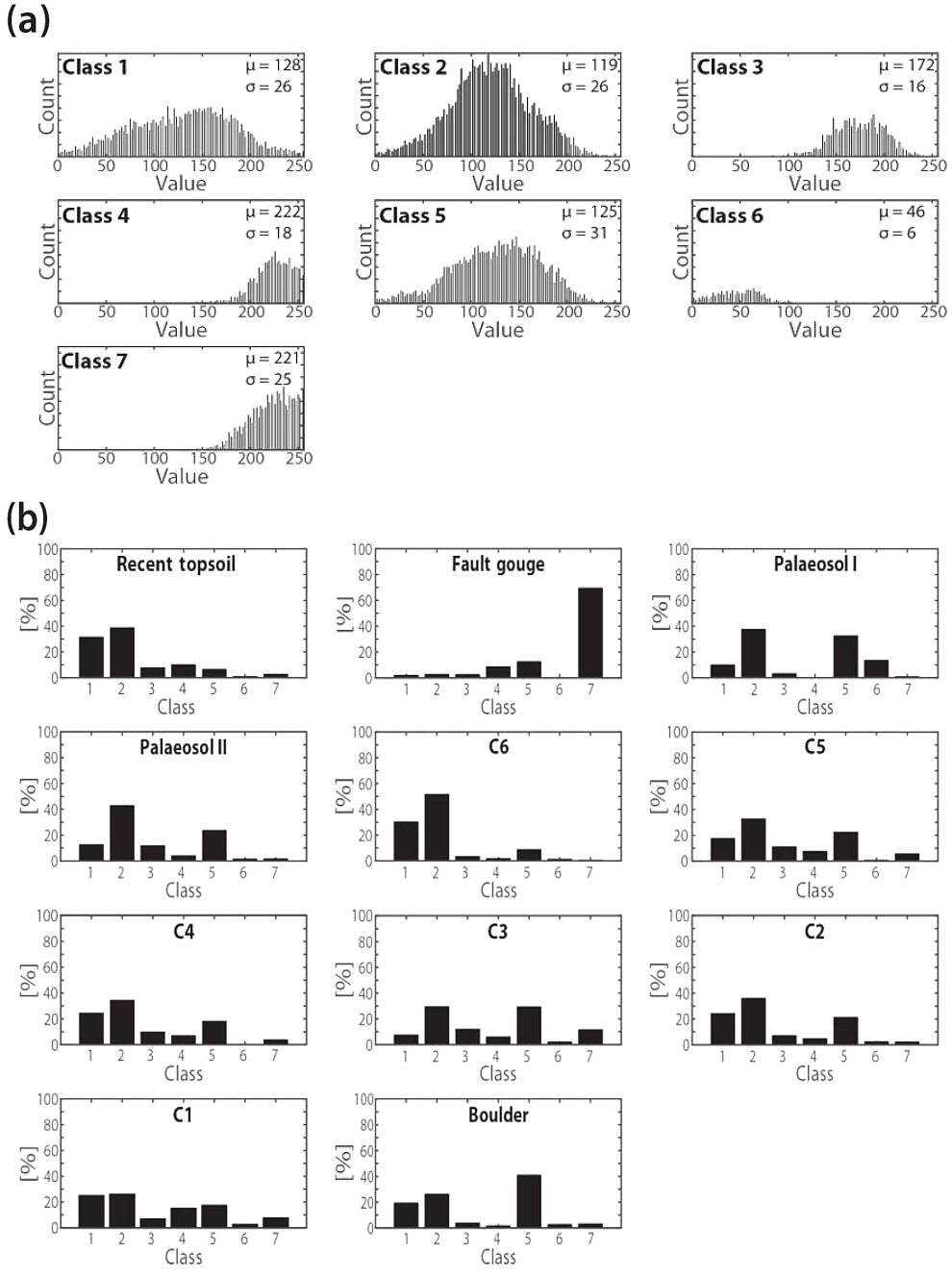

Figure 6. Statistical analysis of two-channel composition image. **(a)** Seven distinct classes were estimated from the unsupervised classification. **(b)** Histograms of representative classes per identified layer. Either the majority of a mapped layer is filled up by one class (e.g. fault gouge) or by a certain composition of two or three classes (e.g. palaeosol II and C6).

Except for C6, which is well represented to around 80 % by class 1 (31 %) and 2 (52 %), and C1, which appears as a unsorted collection of classified responses, the remaining colluvial lithologies appear with similar ratios, especially classes 1, 2, and 5. In a quantitative way no distinction can be recognised. Also, large-scale clustering of classes within the layers is absent. However, arrangements, especially of class 7, are obvious and coincide with coarse-grained gravels within the colluvium. Within C3, a micro-cluster of approximately 25 pixels is arranged along a slightly bent line, dipping about 50° towards the footwall. A similar arrangement of class 7 with an even smaller cluster (3×3 pixels) and wider spread is indicated in C5, dipping 15° towards the footwall. Furthermore, the surrounding matrix is slightly

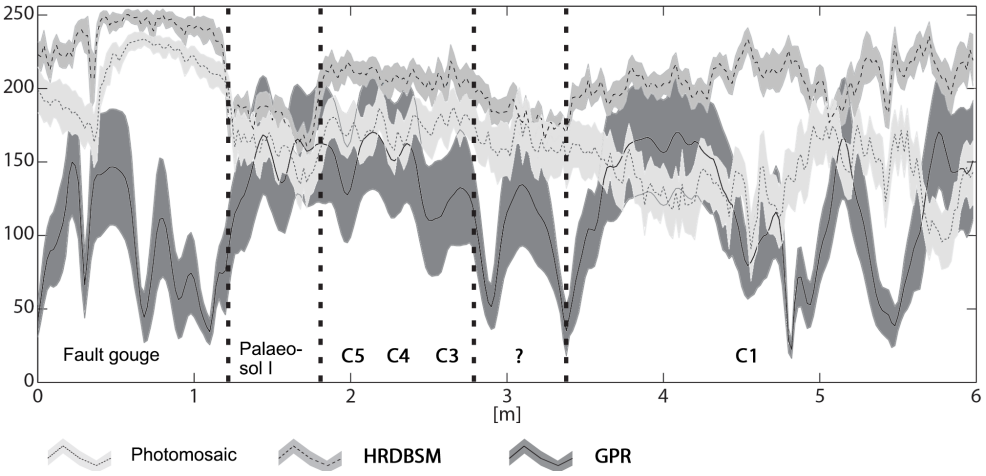

Figure 7. Varying reflectance of electromagnetic waves along the trench wall. Transitions between individual layers are depicted by drastic changing shapes of reflectance spectra. The error range is given by the standard deviation of each sample.

more expressed by class 5 in C5, whereas C3 has, subjectively, no preferred matrix content (Fig. 5). Alterations are expected to decrease with increasing depth. Dependent on rock composition and mean annual precipitation, the formation of new minerals is commonly related to depth from surface. C4 does not show any spectroscopical attribute except for a complete absence of class 6 and low-range greyscale values (see Fig. 6a). Clasts or large boulders protruding out of the trench wall are represented by intermediate value range class 5 on top and wide value range class 1 at the bottom (Fig. 5c).

4.1.3 GPR data interpretation

Using the trench log and multispectral information enables radar facies to be distinguished. Figure 7 confirms the distinction of individual layers by comparison of reflected electromagnetic signal intensity. Reflections of visible and near-infrared light within certain zones that fit with trace increment and dimensions of the GPR system (30×2 cm) were sampled and correlated with the radar's first arrival. As the vertical resolution is a quarter of the wavelength λ (here: 30–40 cm), we averaged reflection amplitudes for 9 cm into depth per trace.

A good correlation between backscattered signals of both passive and active methods is obvious in some parts. A significant contrast in all GPR images is traced by the abrupt transition from fault gouge to palaeosol I (see Figs. 5c, 7). Where reflections of visible and near-infrared light are intense on the surface of the fault gouge exposure, they rapidly decrease in signal strength on the palaeosol surface. The opposite reflectance behaviour is observed for radar reflections in the very shallow subsurface; the first lithological transition is characterised by the change of low to moderate reflection amplitudes in the fine-grained homogeneous fault gouge to higher reflection intensities from heterogeneous palaeosol I.

Moderate reflectance with intermediate variance designates the exposure of palaeosol I. A slightly decreasing trend is obvious within this section just before an abrupt rise in both visible and near-infrared light reflection values. This changeover is not obvious from GPR mean values. However, the value range given by the standard deviation of each sample has a wider reach than in the previous section (Fig. 7). Moreover, there is little distinction between individual colluvial deposits from GPR reflection amplitudes.

As previously stated, the HRDBSM shows an unrecognised feature in the middle of the trench exposure. A change is proven by a drastic drop in reflections from the GPR signal approximately 3 m from the fault plane. In the same position there is also a minor photomosaic and HRDBSM value decline. Thus, a conspicuous progression similar to a Gaussian bell-shaped curve in the middle of a data set is obvious.

Layer C1 is not individually considered since the coupling of the antenna on heavily weathered cemented material with rugged surface relief was not sufficient. However, other transitions recognised in trench log and imaging spectroscopy can be traced in GPR images. This then leads to a 3-D model of coseismic features within the hanging wall (Fig. 8). Seven out of the ten (boulders are not included as an individual layer) previously mapped units plus the limestone fault plane to the west and the adjacent loose material to the east can be traced at depth using GPR.

The 3-D interpretation from GPR images visualises the continuation of distinct layers observed from multispectral analysis into depth. The limestone fault plane and fault gouge clearly differ in GPR images. Also, the cemented colluvium C1 is characterised by continuous and high-amplitude reflections. Coarse-grained components within other colluvial layers are represented as signal scattering hyperbolae within homogeneous matrix facies. However, a distinction between C4, C5, and C6 could not be done with these data. The two

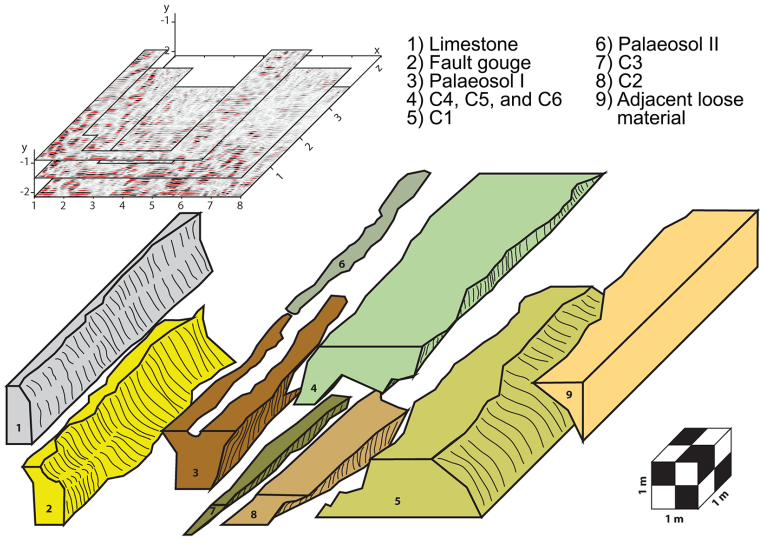

Figure 8. 3-D reconstruction of differing layers within the outcrop from GPR image interpretation. Partial reflection of radar waves on layer contacts leads to significant backscatter signals at depths down to approximately 3 m.

palaeosols differ in the recorded intensity of the reflected electromagnetic waves. Where palaeosol I is characterised by high amplitude reflections, palaeosol II contains only minor reflection hyperbolae caused by small clasts within the homogeneous matrix.

4.2 The Kaparelli Fault, Gulf of Corinth

The description of the Kaparelli Fault trench follows the lithological designations of Kokkalas et al. (2007). The hanging wall and footwall of the Kaparelli Fault are clearly separated by a 70–80° south dipping fault zone (Fig. 1b). This zone is characterised by a chaotic assemblage of sheared deposits and material from surrounding or overlying units that has fallen into cracks and fissures. The footwall consists of multi-coloured pebbly-cobbly gravel deposits with a wide range of coarse-grained subangular to well-rounded clasts in a silty cemented matrix. The hanging-wall block comprises thick deposits of sandy silt (loess deposits) with many steeply dipping fissure fills, some cutting the entire trench wall and others only partly. The fissure width ranges from around 10 to over 80 cm and are filled with subangular to rounded gravel deposits in a silty matrix (Fig. 9a).

The trench log, calibrated using the results from Kokkalas et al. (2007), correlates well with the results from imaging spectroscopy (Fig. 9a). Coarse-grained parts of the exposure to the northern end exhibit a widespread range of greyscale values in both the photomosaic and HRDBSM. Due to a grain size in the order of tens of centimetres and the resulting rough relief, shadows are generated in such a way that significantly influences the colour texture of the photomosaic and the backscattered signal. However, a distinct transition to a silty-sand unit, which prior to this study was described as the fault zone of the 1981 rupture event (Kokkalas et al., 2007), is very clear. Few and much smaller clasts in this unit (diameter is about 1 cm, $< 15\,\%$) and a homogeneous matrix have led to a uniform display in the false colour image. This composition of concurrent greyscale values in the photomosaic and HRDBSM occurs three times in constant offsets along the trench exposure. Pure silt underlies the silty sand. A fissure fill structure of pebbly gravel, dipping about 70° to the south, separates the two blocks of silty-sand and silt layers. Again, a rougher relief leads to a large range of backscattered signal values from both active and passive systems. However, sharp delimitations of juxtaposed lithological units based on their spectroscopic appearance are clear and discernible. A buried soil horizon and a colluvial wedge resulting from the 1981 surface-rupturing event (Kokkalas et al., 2007) are visible and clearly textured by a certain composition of greyscale values.

In Fig. 9b, a 3-D reconstruction from GPR images of the trench wall shows that exposed structures do not only occur on the surface but are also traceable into the hanging wall. Using layer differentiation from imaging spectroscopy helps to recognise certain radar facies even when there are only subtle distinctions. Major components of the trench wall are identified in individual GPR images. Their 3-D extension information is assembled by interpolating between multiple overlaying GPR images. Hence, information on continuation into depth as well as the varying thicknesses of individual layers is gathered. For instance, the colluvial wedge only has a minor variation in its thickness to 2 m penetration depth. The estimated average height for this unit is 0.6 m. This correlates to palaeoevent magnitudes of $M = 6.5$ (Reiss et al., 2003) which is comparable to previous ruptures (Kokkalas et al., 2007). Adjacent units that differ by huge

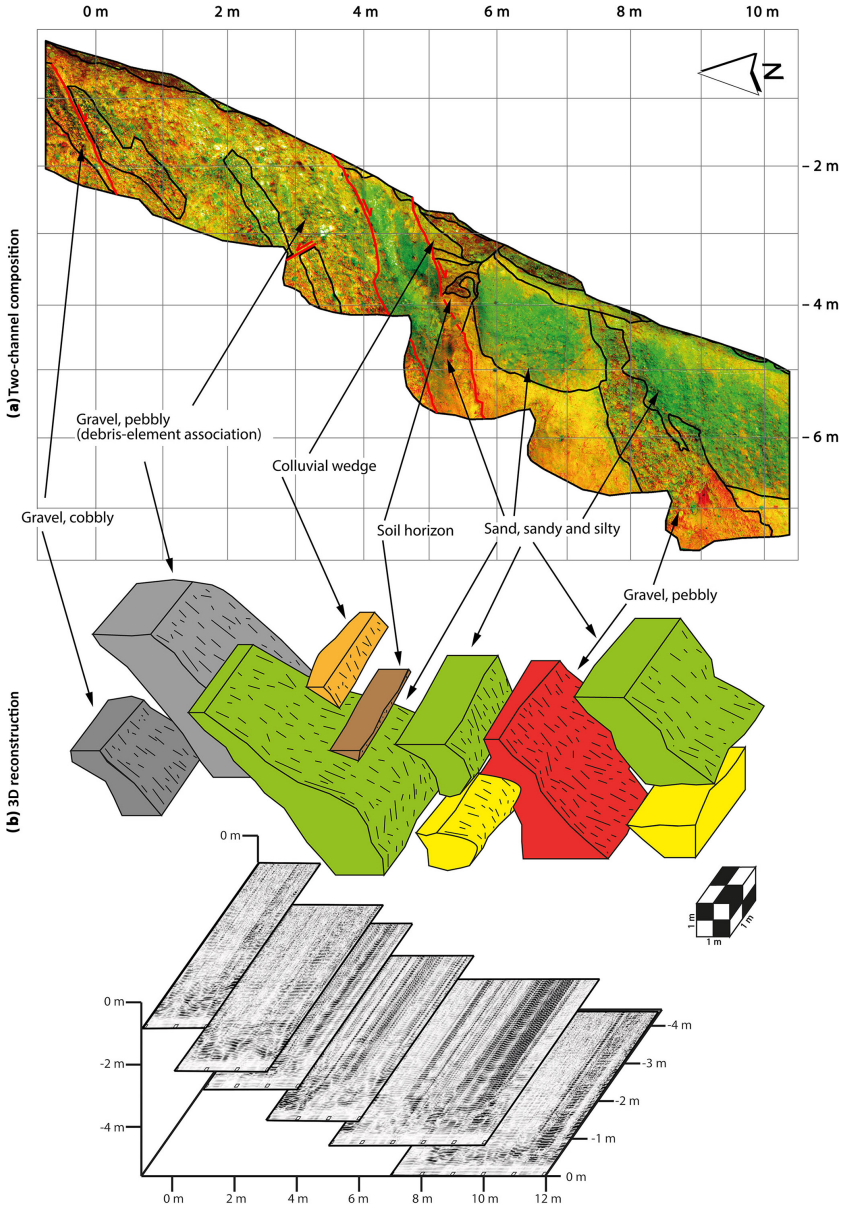

Figure 9. Results from the Kaparelli Fault trench site from Kokkalas et al. (2007). **(a)** Two-channel composition from multispectral approach. Red and green are 100 % different whereas yellow colouring represents intermediate correspondence of both channels. The trench log (black lines) fits with the multispectral cluster of a certain composition. **(b)** 3-D reconstruction of the trench exposure. Recorded thickness of the colluvial wedge from 1981 is about 0.6 m.

grain-size contrasts, like sand and silt next to gravel units, are easy to recognise. Coarse components produce chaotic reflections, while fine-grained units of homogenous material appear with even and quasi-parallel reflections. Thus, the very fine-grained silty clay parts produce fewer reflections than those of pure sand. The unit of debris–element association contains poorly sorted coarse-sized gravels that are expressed by a wavy reflection pattern that does not appear in the hanging wall in the south.

5 Discussion

Trenching investigations have been one of the established methods in palaeoseismic research for the last decades. However, the outcome is highly dependent on the ability of the trench logger to define mappable units and the influence of sunlight since only visual appearance is used to make decisions on individual layer distinction. Furthermore, producing an accurate log and interpretation requires experience and excellent sketching skills. This process can be enhanced using the outcome of a numerical and multispectral view of the

palaeoseismic exposure, which allows quantitative information (reflectivity of electromagnetic waves at different spectra at certain materials) to be assigned to mapped units within the trench wall.

There are some significant disadvantages of passive data collection imaging techniques. These are mainly due to differing angles of illumination because the trench exposure is not a perfectly even surface at all scales; at larger scales surface undulations dramatically increase. Thus, the lightest parts in the photomosaic, visualised for the Sfaka road cut as class 7 with an average value of 221, mainly represent a high matrix luminance and the top (bright) sides of boulders and clasts. Rectification and parallax effects yield an additional error in the order of a few centimetres. However, those effects can be used in structure from motion applications to speed up data collection and improve photomosaic quality as shown by Reitman et al. (2015). High-resolution 3-D images and the near-infrared backscatter signal from t-LiDAR provide information on the physical properties of materials. Colour, matrix, surface roughness and orientation, and varying water content influence the t-LiDAR backscatter signal. A multispectral approach, using unsupervised clustering on both spectra, supports the results from the trench log and complements the findings. Thereby, a distinct layer signature given by particular compositions of effecting classes allows adjacent stratigraphic units to be differentiated. Some areas within the multispectral image lack evidence for distinct spectroscopical characteristics. However, these areas can still be defined when they are adjacent to areas with static characteristics; the boundary between two areas is clearly defined as long as one area can be classified using the unsupervised clustering. Therefore, a spectroscopically inconspicuous and completely heterogeneous area surrounded by regions with static characteristics is still sufficiently confined. Within a given error range due to manual gridding on the trench wall, georectification, and blending pixels of the photomosaic data, the results show many resemblances to the manually drawn trench log.

The results of the imaging spectroscopy verified the lithology of the trench wall, and the resulting image from the unsupervised classification serves as a calibration factor for GPR measurements. Due to the GPR's resolution being about 0.1 m, the calibration is necessary to recognise and interpret minor differences in sedimentological compositions. This method allows more accurate calculations of mean geometric layer thicknesses to be made, which are needed to correlate the amount of vertical offset caused by a specific surface-rupturing event. Information on the average height of a colluvial wedge can be estimated from the in-depth data and then be used to estimate palaeomagnitudes (e.g. Reiss et al., 2003). The quality of the 3-D GPR image and its interpretation depends on well-structured data acquisition and processing, as well as on the experience of the operator. The coupling of the antenna to the surface is decreased on bumpy surfaces, which leads to lower quality data. Moreover, the reference grid on the surface poses a source for stumbling. However, the grid is needed to fuse the geophysical data with remotely collected data and to locate the GPR images in 3-D space. An alternative to a grid made of string is colour spray to mark locations for orientation; but these would have a significant impact on the results from imaging spectroscopy. When the survey is accurately planned and organised, good results can be obtained which allow a 3-D interpretation of sedimentary features to between 2 and 3 m depth within the trench wall.

The biggest disadvantage of the presented workflow is by far the effect of sediment moisture content on reflectance, both in the multispectral analysis and GPR survey. For the multispectral analysis, there is not only darkening of the sediments, which leads to an overall reduction of reflectance, but significant partial absorption at wavelengths near 1.4 and 1.9 µm is also common (Lobell and Asner, 2002; Ragona et al., 2006). Moreover, water content in a given medium leads to distortion effects and high attenuations of electromagnetic waves (Neal, 2004; Schrott and Sass, 2008). However, for conditions when the moisture content is similar throughout the trench wall, water absorptions should not affect the correlations because reflectance along the wall should be affected uniformly. Ragona et al. (2006) have shown that identifying stratigraphy with samples that maintain high amounts of their original moisture content is possible; however, we reiterate the authors' suggestion to consider necessary approaches to minimise changing reflectance. Indeed, the herein presented workflow was successfully tested on normal faults vertically displacing carbonatic bedrock from mostly postglacial colluvial sediments. Therefore, it can be suggested that this technique can only be applied in semi-arid to arid regions such as the Mediterranean or the western USA, where the sediment moisture content is relatively low, at least for a couple of months per year. However, the multispectral analysis and classification does not incorporate layer orientations and can therefore be applied not only on bedrock normal faults, but on any kind of layer discontinuity separating two individual electromagnetically responding facies. Furthermore, the presented technique is robust in identifying distinct sediments (see Figs. 5, 9). Exposures in humid climates most likely maintain much more water. However, Holocene surface ruptures preserved in the shallow subsurface are capable of clearly showing progressive displacements which can also be detected by differing electromagnetic responses (Grützner et al., 2016).

Other potential error sources using this technique are dependent on the characteristics of the individual trenching sites and the equipment used. Some sites are hard to access because of steepness, height, and/or width of the excavation. Extremely steep or narrow trenches make the installation of the scanning equipment difficult. Exposure heights exceeding usual body heights generate problems for the GPR survey; these can be overcome using ropes and wooden tools to ensure good coupling. Scaffolding usually consists of metal

which may lead to interferences in the GPR image. If the trench wall is not properly prepared in terms of cleaning, or the embedded sediments produce a rough surface because of coarser grain sizes, spectral amplitudes will change because of varying illumination and incident angles. Therefore, the spectroscopic interpretation must take these accompanying effects into account. Moreover, extremely complex sedimentological architectures may cause complicated multi-pathing effects on the radar waves. The presented workflow has basic requirements concerning computing capacities; the collected high-resolution data from conventional photo cameras, t-LiDAR scanning, and GPR measurements engage substantial disk space and random access memory.

One major benefit of this workflow is the storage and future use of the raw data. The majority of palaeoseismic trenches are designed to be closed after field investigations are completed. This means that not only is there no future access to these exposures, but the sedimentological environment of the excavated site is also destroyed. If a trench is left open after field investigations, the trench walls will get degraded and altered by weathering effects. t-LiDAR and GPR measurements provide and store information on the visual appearance of the trench and the reflection properties of different electromagnetic wavebands. The reflectance spectrum at each pixel of an image provides unbiased compositional information. This saved data can always be used for future (re)analyses. Another benefit is the ability to record trench data in hazardous exposures without extensive, time-consuming, and costly safety precautions. Also, as trenches are often only open for limited durations, the logger might not have enough time to accurately sketch and measure components, or he may rush to finish. In these cases, capturing and recording the outcrop in a multidimensional manner (x, y, z coordinates of each data point plus reflectance values of visual and near-infrared light and pseudo-3-D information within the hanging wall) enables efficient productivity and forms a complementary approach.

6 Conclusions

Identifying and mapping individual lithological units along a palaeoseismological exposure in accordance with colour and matrix specifications, as well as sedimentary structures and soil formations, are core competencies of palaeoseismic trenching studies. However, the accuracy and quality of the log and interpretation is highly dependent on the experience of the trench logger, and is thus subjectively influenced. Hence, minor differences in lithological description from expert to expert are expected, especially if one logger has access to no more than a photomosaic. In order to prove whether conventional trench logging methods used to map coseismic features in a palaeoseismic trench wall can be objectively enhanced, we created an accurate digital version of the exposure and its physical properties. This was done by combining routine logging with vertical GPR measurements and imaging spectroscopic approaches from normalised photomosaics and high-resolution t-LiDAR backscatter models. Both the studied palaeoseismic exposures, on Crete and mainland Greece, exhibit sedimentary structures whose constituent parts and shape are essential information for a palaeoseismic reconstruction.

After the conventional trench logging was completed, t-LIDAR scans were undertaken at close range. The near-infrared backscattered signal was combined with a luminance-bearing photomosaic of the same trench wall. Statistical and classification techniques reproduce an objective digital copy of a palaeoseismic trench log. In order to define distinct units, four options to characterise and differentiate individual layers by imaging spectroscopy can be registered:

- significant dominance of a certain class within a distinct layer
- certain composition with spatial clustering
- certain composition with certain arrangements
- distinct borders between individual layers, although one or both are not determined by applied statistics.

Subtle or invisible features are enhanced and become part of a quantitative analysis, and comparisons of units using their reflectance on certain wavelengths (see also Ragona et al., 2006) can be carried out. Our results show that based on distinct layers in the trench log, in combination with the outcome of imaging spectroscopy, a 3-D interpretation of GPR data carried out vertically on the trench wall is possible. Hence, the spatial extent of palaeoseismic features can be traced within the trench wall. The resulting 3-D model from the GPR provides information on representative layer thicknesses, displacements, and geometries. This is highly beneficial since it minimises misinterpretation due to cutting effects.

To extract such fault-specific information is not only crucial for identification and mapping active faults but also depicts complementary input for seismic hazard assessment by extracting more accurate magnitudes of palaeoearthquakes (Papanikolaou et al., 2015). The use of t-LiDAR has become a major tool to obtain such data. So far, this modern technology has been used for fault mapping at regional- to micro-scale coverage with up to millimetre resolution (e.g. Arrowsmith and Zielke, 2009; Begg and Mouslopoulou, 2010; Wilkinson et al., 2010, 2015; Bubeck et al., 2015). Further, the visualisation of bare-earth topography at a regional scale (Cunningham et al., 2006) and the detection of roughness changes along fault scarps (Wiatr et al., 2015) are scopes of application. Here another approach of the use of t-LiDAR in palaeoseismology is presented. Recording and measuring the backscattered signal in the near-infrared band enables the visualisation of usually non-visible electromagnetic waves. The spectral response represents material-specific properties

and gives evidence for differing lithology along the exposure. For seismic hazard assessments, accurate and justified decisions on the interpretation of such data are needed. To further assist, high-resolution GPR profiling visualises the associated sedimentary architecture within the hanging wall and quantifies and qualifies event horizons to estimate palaeomagnitudes and slip rates on active normal faults (Reiss et al., 2003).

The presented workflow does not form an alternative to conventional trench logging since this approach only records complementary data. Information on detailed grain-size distribution along the exposure or the orientation of certain components is not addressed by the workflow. Even photomosaic methods cannot offer required pixel resolution. However, if logistics are difficult and/or the trench wall is hazardous, a t-LiDAR scan and photographs can be applied from outside of the exposure and be used to quickly provide high-resolution data. This forms an alternative data collection method when the opening time is short or when operators cannot stay safely in the trench. The provided data visualise features that are usually not visible, allow decisions on interpreting the seismic history of the fault to be justified, and the spectrum reflectance data provide unbiased measurements that can be (re)processed any time after the trench has been backfilled.

Reconstructing the palaeoseismological history of both trench exposures is not an integral part of this paper. However, the objective of improving individual event horizon recognition using multispectral viewing and 3-D visualisation of GPR images was successfully undertaken. This method can therefore contribute to the accuracy of seismic hazard assessment.

Acknowledgements. We thank Aggelos Pallikarakis from the Agricultural University of Athens for his cooperation and assistance on Crete and in mainland Greece. Silke Mechernich, Lauretta Kärger, Tobias Baumeister, and Alexander Woywode supported our fieldwork. In Pachia Ammos, the Zorbas Taverna is thanked for the loan of equipment and excellent food.

The authors would like to thank Christoph Grützner from Cambridge University for his valuable comments regarding the manuscript.

We are thankful to the anonymous reviewers who provided very useful comments that helped to improve the paper.

Edited by: F. Rossetti

References

Alasset, P.-J. and Meghraoui, M.: Active faulting in the western Pyrénées (France): paleoseismic evidence for late Holocene ruptures, Tectonophysics, 409, 39–54, 2005.

Ambraseys, N. N. and Jackson, J. A.: Seismicity and associated strain of central Greece between 1890 and 1988, Geophys. J. Int., 101, 663–708, 1990.

Arrowsmith, J. R. and Zielke, O.: Tectonic geomorphology of the San Andreas Fault zone from high resolution topography: An example from the Cholame segment, Geomorphology, 113, 70–81, 2009.

Begg, J. G. and Mouslopoulou, V.: Analysis of late Holocene faulting within an active rift using lidar, Taupo Rift, New Zealand, J. Volcanol. Geoth. Res., 190, 152–167, 2010.

Benedetti, L., Finkel, R., Papanastassiou, D., King, G., Armijo, R., Ryerson, F., Farber, D., and Flerit, F.: Post-glacial slip history of the Sparta fault (Greece) determined by ^{36}Cl cosmogenic dating: Evidence for non-periodic earthquakes, Geophys. Res. Lett., 29, 87-1–87-4, doi:10.1029/2001GL014510, 2002.

Benedetti, L., Finkel, R., King, G., Armijo, R., Papanastassiou, D., Ryerson, F. J., Flerit, F., Farber, D., and Stavrakakis, G.: Motion on the Kaparelli fault (Greece) prior to the 1981 earthquake sequence determined from ^{36}Cl cosmogenic dating, Terra Nova, 15, 118–124, 2003.

Brodu, N. and Lague, D.: 3-D terrestrial lidar data classification of complex natural scenes using a multi-scale dimensionality criterion: Applications in geomorphology, ISPRS J. Photogramm., 68, 121–134, 2012.

Bubeck, A., Wilkinson, M., Roberts, G. P., Cowie, P. A., McCaffrey, K., Phillips, R., and Sammonds, P.: The tectonic geomorphology of bedrock scarps on active normal faults in the Italian Apennines mapped using combined ground penetrating radar and terrestrial laser scanning, Geomorphology, 237, 38–51, 2015.

Chow, J., Angelier, J., Hua, J.-J., Lee, J.-C., and Sun, R.: Paleoseismic event and active faulting: from ground penetrating radar and high-resolution seismic reflection profiles across the Chihshang Fault, eastern Taiwan, Tectonophysics, 333, 241–259, 2001.

Christie, M., Tsoflias, G. P., Stockli, D. F., and Black, R.: Assessing fault displacement and off-fault deformation in an extensional tectonic setting using 3-D ground-penetrating radar imaging, J. Appl. Geophys., 68, 9–16, 2009.

Cunningham, D., Grebby, S., Tansey, K., Gosar, A., and Kastelic, V.: Application of airborne LiDAR to mapping seismogenic faults in forested mountainous terrain, southeastern Alps, Slovenia, Geophys. Res. Lett., 33, L20308, doi:10.1029/2006GL027014 2006.

Demanet, D., Renardy, F., Vanneste, K., Jongmans, D., Camelbeeck, T., and Meghraoui, M.: The use of geophysical prospecting for imaging active faults in the Roer Graben, Belgium, Geophysics, 66, 78–89, 2001.

Ercoli, M., Pauselli, C., Frigeri, A., Forte, E., and Federico, C.: "Geophysical paleoseismology" through high resolution GPR data: A case of shallow faulting imaging in Central Italy, J. Appl. Geophys., 90, 27–40, 2013.

Gaki-Papanastassiou, K., Karymbalis, E., Papanastassiou, D., and Maroukian, H.: Quaternary marine terraces as indicators of neotectonic activity of the Ierapetra normal fault SE Crete (Greece), Geomorphology, 104, 38–46, 2009.

Grützner, C., Reicherter, K., Hübscher, C., and Silva, P. G.: Active faulting and neotectonics in the Baelo Claudia area, Campo de Gibraltar (southern Spain), Tectonophysics, 554–557, 127–142, 2012.

Grützner, C., Barba, S., Papanikolaou, I. D., and Pérez-López, R.: Earthquake geology: science, society and critical facilities, Ann. Geophys.-Italy, 56, S0683, doi:10.4401/ag-6503, 2013.

Grützner, C., Fischer, P., and Reicherter, K.: Holocene surface ruptures of the Rurrand Fault, Germany-insights from palaeoseismology, remote sensing and shallow geophysics, Geophys. J. Int., 204, 1662–1677, 2016.

Guidoboni, E. and Ebel, J. E.: Earthquakes and tsunamis in the past: A guide to techniques in historical seismology, Cambridge University Press, Cambridge, UK, New York, xi, 604 pp., 2009.

Höfle, B. and Pfeifer, N.: Correction of laser scanning intensity data: data and model-driven approaches, ISPRS J. Photogramm., 62, 415–433, 2007.

Hu, H., Fernandez-Steeger, T. M., Dong, M., and Azzam, R.: Numerical modeling of LiDAR-based geological model for landslide analysis, Automat. Construct., 24, 184–193, 2012.

Jackson, J. A., Gagnepain, J., Houseman, G., King, G., Papadimitriou, P., Soufleris, C., and Virieux, J.: Seismicity, normal faulting, and the geomorphological development of the Gulf of Corinth (Greece): the Corinth earthquakes of February and March 1981, Earth Planet. Sc. Lett., 57, 377–397, 1982.

Jones, L. D.: Monitoring landslides in hazardous terrain using terrestrial LiDAR: an example from Montserrat, Q. J. Eng. Geol. Hydroge., 39, 371–373, 2006.

Jörg, P., Fromm, R., Sailer, R., and Schaffhauser, A.: Measuring snow depth with a terrestrial laser ranging system, International Snow Science Workshop, 1–6 October 2006, Telluride, CO, USA, 452–460, 2006.

Keller, E. A. and Rockwell, T. K.: Tectonic Geomorphology, Quaternary chronology, and Paleoseismicity, in: Tectonic Geormophology, Quaternary Chronology, and Paleoseismicity, Developments and Applications of Geomorphology, edited by: Costa, J. E. and Fleisher, P. J., Springer, Berlin, Heidelberg, 203–239, 1984.

Kokkalas, S. and Koukouvelas, I. K.: Fault-scarp degradation modeling in central Greece: the Kaparelli and Eliki faults (Gulf of Corinth) as a case study, J. Geodyn., 40, 200–215, 2005.

Kokkalas, S., Pavlides, S., Koukouvelas, I. K., Ganas, A., and Stamatopoulos, L.: Paleoseimicity of the Kaparelli fault (eastern Corinth Gulf): evidence for earthquake recurrence and fault behaviour, Boll. Soc. Geol. Ital., 126, 387–395, 2007.

Le Pichon, X. and Angelier, J.: The hellenic arc and trench system: a key to the neotectonic evolution of the eastern mediterranean area, Tectonophysics, 60, 1–42, 1979.

Lobell, D. B. and Asner, G. P.: Moisture effects on soil reflectance, Soil Sci. Soc. Am. J., 66, 722–727, doi:10.2136/sssaj2002.7220, 2002.

Lyon-Caen, H., Armijo, R., Drakopoulos, J., Baskoutass, J., Delibassis, N., Gaulon, R., Kouskouna, V., Latoussakis, J., Makropoulos, K., Papadimitriou, P., Papanastassiou, D., and Pedotti, G.: The 1986 Kalamata (South Peloponnesus) Earthquake: detailed study of a normal fault, evidences for east–west extension in the Hellenic Arc, J. Geophys. Res., 93, 14967, doi:10.1029/JB093iB12p14967, 1988.

Machette, M. N.: Active, capable, and potentially active faults – a paleoseismic perspective, J. Geodyn., 29, 387–392, 2000.

Mariolakos, I. and Papanikolaou, D. J.: The Neogene basins of the Aegean Arc from the Paleogeographic and the Geodynamic point of view, in: Proc. Int. Symp. H. E. A. T., Athens, Greece, 8–10 April 1981, 383–399, 1981.

McCalpin, J.: Paleoseismology, 2nd Edn., Academic Press, Burlington, MA, International Geophysics Series, 95, 613 pp., 2009.

McKenzie, D.: Active tectonics of the Mediterranean region, Geophys. J. Roy. Astr. S., 30, 109–185, 1972.

Neal, A.: Ground-penetrating radar and its use in sedimentology: principles, problems and progress, Earth-Sci. Rev., 66, 261–330, 2004.

Papanikolaou, D. J. and Royden, L. H.: Disruption of the Hellenic arc: late Miocene extensional detachment faults and steep Pliocene-Quaternary normal faults – or what happened at Corinth?, Tectonics, 26, TTC5003, doi:10.1029/2006TC002007, 2007.

Papanikolaou, I. D., van Balen, R., Silva, P. G., and Reicherter, K.: Geomorphology of active faulting and seismic hazard assessment: new tools and future challenges, Geomorphology, 237, 1–13, 2015.

Papazachos, B. C., Comnakis, P. E., Karakaisis, G. F., Karakostas, B. G., Papaioannou, C., Papazachos, C. B., and Scordilis, E. M.: A Catalogue of Earthquakes in Greece and Surrounding Area for the Period 550 BC–1999, Publication of the Geophysical Laboratory, University of Thessaloniki, Thessaloniki, Greece, 1, 333 pp., 2000.

Ragona, D., Minster, B., Rockwell, T., and Jussila, J.: Field imaging spectroscopy: a new methodology to assist the description, interpretation, and archiving of paleoseismological information from faulted exposures, J. Geophys. Res., 111, B10309, doi:10.1029/2006JB004267, 2006.

Reicherter, K.: Paleoseismologic advances in the Granada Basin (Betic Cordilleras, southern Spain), Paleoseismology of Spain, Acta Geologica Hispanica, 36, 267–281, 2001.

Reicherter, K., Jabaloy, A., Galindo-Zaldívar, J., Ruano, P., Becker-Heidmann, P., Morales, J., Reiss, S., and González-Lodeiro, F.: Repeated palaeoseismic activity of the Ventas de Zafarraya fault (S Spain) and its relation with the 1884 Andalusian earthquake, Int. J. Earth Sci., 92, 912–922, 2003.

Reicherter, K., Michetti, A. M., and Barroso, P. G. S.: Palaeoseismology: historical and prehistorical records of earthquake ground effects for seismic hazard assessment, Geological Society, London, Special Publications, 316, 1–10, 2009.

Reiss, S., Reicherter, K., and Reuther, C.-D.: Visualization and characterization of active normal faults and associated sediments by high-resolution GPR, Geological Society, London, Special Publications, 211, 247–255, 2003.

Reitman, N. G., Bennett, S. E. K., Gold, R. D., Briggs, R. W., and DuRoss, C. B.: High-Resolution Trench Photomosaics from Image-Based Modeling: Workflow and Error Analysis, B. Seismol. Soc. Am., 105, 2354, doi:10.1785/0120150041, 2015.

Sabins, F. F.: Remote Sensing: Principles and Interpretation, 3rd Edn., edited by: Freeman, W. H., W. H. Freeman Electronic Publishing Center/Andrew Kudlacik, New York, USA, 494 pp., 1997.

Schrott, L. and Sass, O.: Application of field geophysics in geomorphology: advances and limitations exemplified by case studies, Geomorphology, 93, 55–73, 2008.

Sieh, K. E.: Prehistoric large earthquakes produced by slip on the San Andreas Fault at Pallett Creek, California, J. Geophys. Res., 83, 3907, doi:10.1029/JB083iB08p03907, 1978.

Stewart, I. and Hancock, P.: Scales of structural heterogeneity within neotectonic normal fault zones in the Aegean region, J. Struct. Geol., 13, 191–204, 1991.

Stucchi, M., Albini, P., Mirto, C., and Rebez, A.: Assessing the completeness of Italian historical earthquake data, Ann. Geophys.-Italy, 47, 659–673, 2004.

Stucchi, M., Rovida, A., Gomez Capera, A. A., Alexandre, P., Camelbeeck, T., Demircioglu, M. B., Gasperini, P., Kouskouna, V., Musson, R. M. W., Radulian, M., Sesetyan, K., Vilanova, S., Baumont, D., Bungum, H., Fah, D., Lenhardt, W., Makropoulos, K., Martinez Solares, J. M., Scotti, O., Živčić, M., Albini, P., Batllo, J., Papaioannou, C., Tatevossian, R., Locati, M., Meletti, C., Viganò, D., and Giardini, D.: The SHARE European Earthquake Catalogue (SHEEC) 1000–1899, J. Seismol., 17, 523–544, 2013.

Tucker, C. J.: Red and photographic infrared linear combinations for monitoring vegetation, Remote Sens. Environ., 8, 127–150, 1979.

Vanneste, K., Verbeeck, K., and Petermans, T.: Pseudo-3-D imaging of a low-slip-rate, active 3 normal fault using shallow geophysical methods: The Geleen fault in the Belgian Maas River valley, Geophysics, 73, B1, 2008.

Wallace, R. E.: Active Tectonics: Impact on Society, The National Academies Press, Washington, DC, 1986.

Wells, D. L. and Coppersmith, K. J.: New empirical relationships among magnitude, rupture length, rupture width, rupture area, and surface displacement, B. Seismol. Soc. Am., 84, 974–1002, 1994.

Wesnousky, S. G.: Earthquakes, quaternary faults, and seismic hazard in California, J. Geophys. Res., 91, 12587–12631, 1986.

Wiatr, T., Papanikolaou, I., Fernández-Steeger, T., and Reicherter, K.: Bedrock fault scarp history: insight from t-LiDAR backscatter behaviour and analysis of structure changes, Geomorphology, 228, 421–431, 2015.

Wilkinson, M., McCaffrey, K. J. W., Roberts, G., Cowie, P. A., Phillips, R. J., Michetti, A. M., Vittori, E., Guerrieri, L., Blumetti, A. M., Bubeck, A., Yates, A., and Sileo, G.: Partitioned postseismic deformation associated with the 2009 Mw 6.3 L'Aquila earthquake 18 surface rupture measured using a terrestrial laser scanner, Geophys. Res. Lett., 37, L10309, doi:10.1029/2010GL043099, 2010.

Wilkinson, M., Roberts, G. P., McCaffrey, K., Cowie, P. A., Faure Walker, Joanna P., Papanikolaou, I., Phillips, R. J., Michetti, A. M., Vittori, E., Gregory, L., Wedmore, L., and Watson, Z. K.: Slip distributions on active normal faults measured from LiDAR and field mapping of geomorphic offsets: an example from L'Aquila, Italy, and implications for modelling seismic moment release, Geomorphology, 237, 130–141, doi:10.1016/j.geomorph.2014.04.026, 2015.

Woessner, J. and Wiemer, S.: Assessing the Quality of Earthquake Catalogues: Estimating the 25 Magnitude of Completeness and Its Uncertainty, B. Seismol. Soc. Am., 95, 684–698, 2005.

Yeats, R. S. and Prentice, C. S.: Introduction to special section: paleoseismology, J. Geophys. Res., 101, 5847–5853, doi:10.1029/95JB03134, 1996.